Environmental Science Advances

PAPER

View Article Online
View Journal | View Issue

Cite this: *Environ. Sci.: Adv.*, 2024, **3**, 97

Optimizing the electronic configuration of h-BN for boosting the photocatalytic transformation of acid gases under visible light†

Hao Yang,[ab] Libin Zeng,[a] Jiali Wang[a] and Can Yang *[a]

Developing the diverse chemical properties and expanding the catalytic performance of boron nitride (BN) materials remains a formidable challenge although it has long been a hot topic of research. Optimizing the electronic configuration of BN is implemented by incorporating heteroatomic carbon, which endows modified BN with features in terms of visible-light response, highly efficient charge separation and available surface-active sites. In addition, it was also found that the introduction of carbon also enhanced the adsorption and activation of BN on reactant molecules using diffuse reflection infrared Fourier transformation spectroscopy (DRIFTS), temperature-programmed desorption (TPD) and electron paramagnetic resonance (EPR) spectroscopy. As expected, carbon-doped boron nitride (BCN) shows remarkable performance in the photocatalytic removal of hydrogen sulfide (H_2S) and nitric oxide (NO). The optimized BCN sample exhibits 99% and 60% of the photocatalytic removal efficiency for 20 ppm H_2S (Flow velocity, 20 mL min^{-1}) and 1 ppm NO (Flow velocity, 500 mL min^{-1}), respectively. This work provides insight into the design of functionalized BN and an exciting approach to handling low-concentration acidic gases.

Received 21st August 2023
Accepted 14th November 2023

DOI: 10.1039/d3va00239j

rsc.li/esadvances

Environmental significance

Handling low-concentration acidic gases (H_2S and NO) in the environment remains a huge challenge because of their low abundance and strong corrosiveness. At present, these acid gases are mainly eliminated by physical adsorption or solution absorption, but these methods often create secondary pollution problems. Therefore, it is significant to develop an efficient and clean treatment process. To this end, we constructed photocatalytic systems for the treatment of these acidic and corrosive gases. This process uses highly efficient photocatalysts with corrosion resistance and clean solar energy as the driving force, allowing no secondary pollutants to be generated throughout the treatment process.

1. Introduction

Acidic gases (H_2S and NO) not only cause huge obstacles to industry but also harm human health and pollute the air.[1] Although very well-established processes, such as the Claus method for H_2S, wet oxidation desulfurization (WOD) for SO_2 and selective catalytic reduction (SCR) for NO_x, have been extensively applied in removing high-concentration acid gases, it is still inevitable that small amounts of acid gases will be discharged into the atmosphere.[2–4] Handling low-concentration acidic gases that are dispersed in the environment poses greater challenges to treatment processes.[5–7] Currently, the main methods for eliminating these low concentrations of acid gases are physical adsorption or solution absorption, but these methods often cause secondary pollution problems. Therefore, it is of great significance to develop an efficient and clean treatment process. Photocatalysis is an emerging technology that has been extensively researched because of its use of cheap and non-polluting solar energy as a driving force.[8–13] In particular, photocatalysis has shown great potential in treating low concentrations of gaseous pollutants in the environment, which generally accomplishes the purification of gaseous pollutants by photolysis or mineralization.[14–16] The top priority in developing efficient photocatalytic schemes is the development of low-cost, highly stable and active catalysts.[17–19] Considering the majority of metal-based catalysts are easily poisoned in sulfur-containing gases because numerous metal atoms easily form strong coordination with sulfur atoms, the development of free-metal catalysts with chemical stability has become a new research trend in photocatalysis of acidic gases.[20,21] Due to its exceptional features including chemical resistance, thermal stability, and unique electronic properties, hexagonal boron nitride (h-BN) has emerged as the subject of research.[22] As a two-

[a]*State Key Laboratory of Photocatalysis on Energy and Environment, College of Chemistry, Fuzhou University, Fuzhou, 350116, P. R. China. E-mail: canyang@fzu.edu.cn*

[b]*College of Chemical Engineering, Fuzhou University, Fuzhou, 350116, P. R. China*

† Electronic supplementary information (ESI) available. See DOI: https://doi.org/10.1039/d3va00239j

dimensional metal-free material, the monolayer structures of h-BN are composed of alternating hexagonal N and B atoms which are similar to the honeycomb structure of graphene. The van der Waals interactions function as the monolayer structures to form a two-dimensional material, endowing BN with high thermal conductivity.[23] However, the B–N electron pairs with higher electronegativity are restricted to the N atoms, resulting in a low degree of delocalization of the B–N bond in comparison to graphene, which is made up of equally contributed C–C bonds.[24] This reduced delocalization feature of the BN electronic configuration caused a large band gap, which greatly limited their applications in catalysis, especially in photocatalysis.

Modifying BN into an excellent photocatalyst with a visible light response is a challenging task because highly stable ceramic properties leave it with limited means of structural modulation. The straightforward strategy is compounding with other semiconductors that have superior light absorption but low photogenerated charge separation efficiency to construct efficient composite photocatalysts, where BN acts as a promoter of photogenerated carriers because of its unique physico-chemical properties.[25,26] And then, the modification of the functional group is approved to be an effective means for improvement of BN light uptake. Predictions of theoretical calculations reveal that the band gap of BN reduced from ~5.5 to ~2.2 eV by hydrogenation of BN terminated edges.[27,28] Subsequent experiments have indicated that functionalizing BN with the –OH group by introducing an in-plane inhibitor allows it to absorb visible light as well.[29] Another effective approach is the introduction of heteroatoms (C, O, F) during the synthesis process to modulate the local electronic structure, which can strengthen the visible-light absorption of BN.[30–32] Among them, carbon-doped boron nitride (BCN) is favored because the matching of C atom sizes to B and N atoms allows easy embedding. As a photocatalyst, BCN has been reported for the decomposition of water into H_2, reduction of CO_2, oxidation of benzyl alcohol, and mineralization of volatile organic compounds (VOCs).[33–36] Incorporating sp^2 carbon in the BN lattice induces a delocalized two-dimensional electron domain in BCN units where the C atom breaks the strongly electronegative B–N bond reducing the band gap of the BCN. Recent studies have shown that carbon induces Lewis acid sites (undercoordinated B sites) and Lewis base sites (undercoordinated N sites) in the BCN as well as forming large specific surface area, facilitating the adsorption and activation of gas molecules.[37] Moreover, these structural base active sites in the BCN chemical structure contribute to resisting the change of catalyst surface state in the acidic gas environment. Therefore, BCN is an encouraging candidate for the treatment of acidic waste gases that benefits from excellent corrosion resistance and easily tunable band structure, but relevant research is very scarce.

In this work, BCN is successfully synthesized by a high-temperature thermal polymerization process. The impacts of carbon on the chemical state, band structure, and photogenerated charge separation efficiency of BCN materials have been comprehensively investigated through a series of characterizations. The adsorption and activation behavior of reactants and photocatalytic mechanism were analyzed by DRIFTS, TPD and EPR spectroscopy, *etc.* Thus, carbon-doped BN (BCN) exhibits outstanding activity and stability for the photocatalytic elimination of acid gas under visible light.

2. Experimental section

2.1 Preparation of samples

Urea (>99.0%), boric acid (>99.0%), and glucose (>99.0%) were obtained from Sinopharm Chemical Reagent (Shanghai, China). All of these materials were used as received without further purification.

For the synthesis of BCN material, 4 g of urea, 2 g of boric acid and 4 g of glucose were thoroughly ground and transferred to a corundum boat. Then, the corundum boat was heated at 1250 °C for 5 h in a high-temperature tube furnace. The entire heating process was carried out under an ammonia atmosphere (250 mL min^{-1}). Once the tube furnace had cooled to room temperature naturally, the system was purged with nitrogen and samples were collected. The BCN samples with different carbon content were obtained by adding different amounts of glucose. The sample with a small amount of glucose (1 g) was named BCN-1, the sample with a moderate amount of glucose (4 g) was named BCN-2, and the sample with excess glucose (10 g) was named BCN-3.

The BN sample was synthesized following the same procedure as for BCN except that no glucose was added.

2.2 Photocatalytic device and procedure

The photocatalytic H_2S removal experiment was carried out using a continuous gas–solid phase reaction device (Scheme 1). In a typical photocatalytic H_2S removal process, 40 mg of catalyst was fixed in a quartz reactor with LED lamp irradiation (40 W, 420 nm). The feed gas includes 20 ppm H_2S gas and 50% standard air and nitrogen as balance gas. The feed gas is flowed under dark conditions for a period of time before the photocatalytic reaction to ensure that it reaches adsorption equilibrium on the catalyst surface. After the reaction, a gas chromatograph equipped with an FPD detector is used to detect the concentrations of gas. The removal efficiency (η) of H_2S was calculated as $\eta = (1 - C/C_0) \times 100\%$, where C and C_0 are the

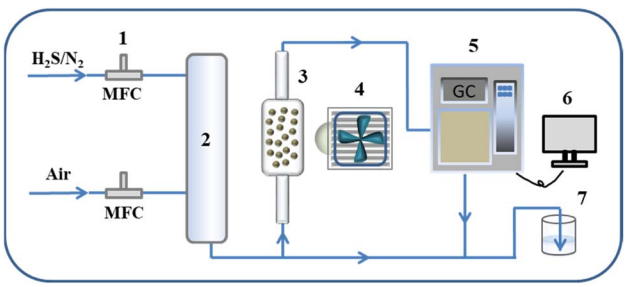

Scheme 1 Schematic diagram of the photocatalytic H_2S removal process. (1) Mass flow controller; (2) gas mixing tank; (3) reactor; (4) light source; (5) gas chromatograph; (6) computer; (7) tail gas collector.

transient and initial concentrations of H_2S, respectively. Finally, the device containing NaOH solution was used at the end of the gas path to absorb the residual sulfur-containing gas.

3. Results and discussion

3.1 The characterization of composition and microstructure

The BCN samples were synthesized by the thermal polymerization method (Fig. 1).[33] The X-ray diffraction (XRD) pattern of BN reveals two peaks at 25° and 42° belonging to the (002) and (001) planes of the graphite structure, respectively (Fig. 2a).[37] The fact that all BCN samples show similar diffraction peaks indicates that the intrinsic structure of BN was not destroyed after incorporating carbon. Meanwhile, the diffraction peaks shift slightly to a low angle and the peak intensity decreases after carbon doping due to the incorporated carbon in the B–N domain.[33] As shown in Fig. 2b, the obvious peaks attributed to the out-of-plane bending vibration of B–N–B (790 cm^{-1}) and in-plane transverse stretching vibration of B–N (1338 cm^{-1}) are observed in the Fourier transform infrared (FTIR) spectrum.[38] Furthermore, the ratios of peak areas of B–N–B and B–N diminish after incorporating carbon. This implies the breaking of the B–N–B bond and the formation of a new B–N unit after carbon incorporates the B–N domain.[36]

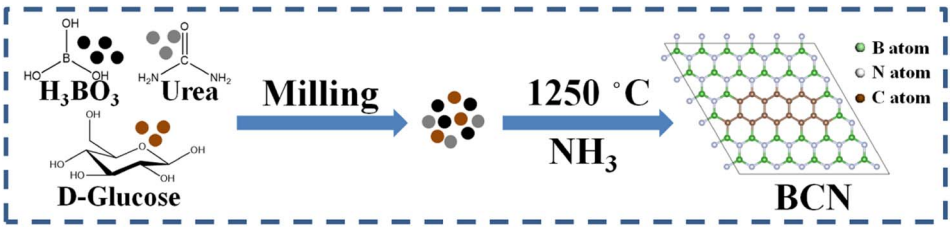

Fig. 1 Schematic diagram of the synthesis of BCN samples.

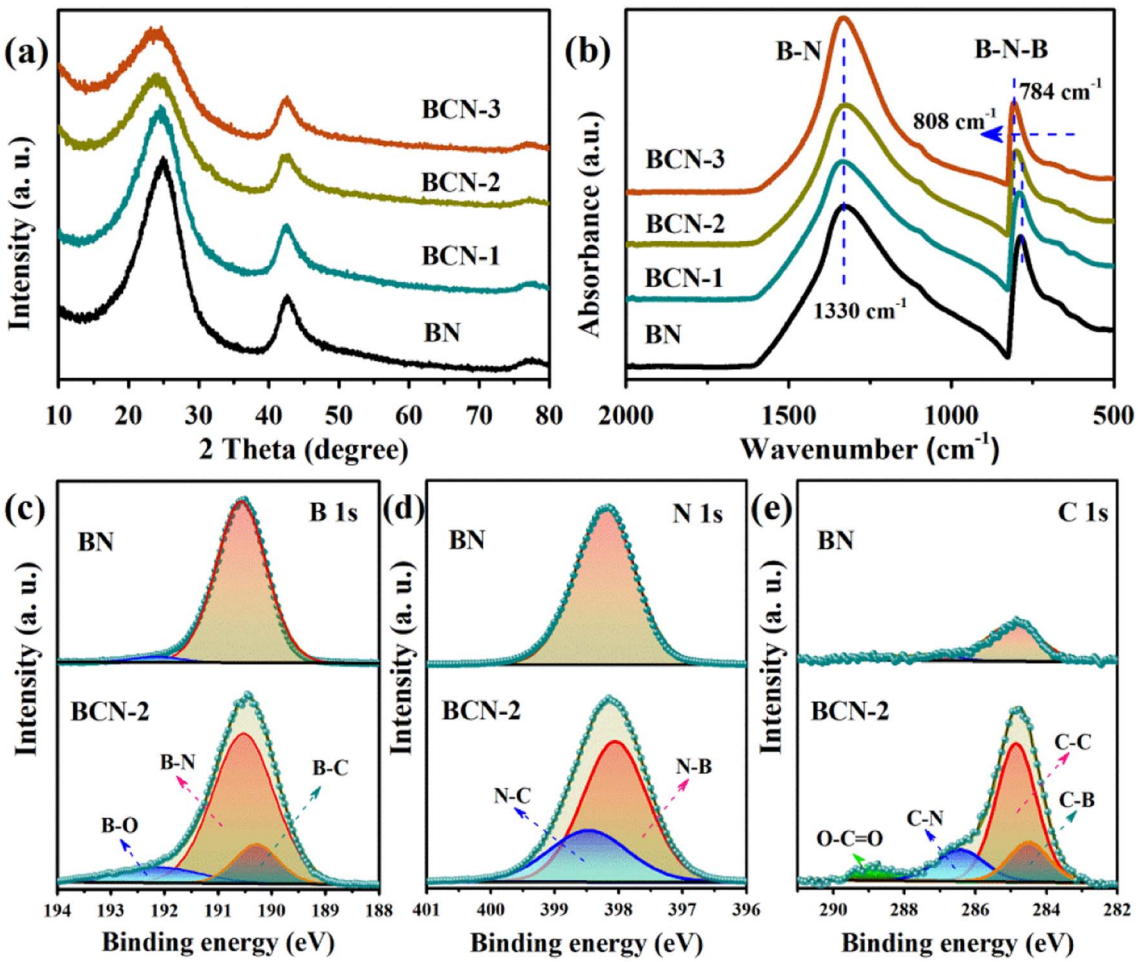

Fig. 2 (a) XRD patterns of all the samples, (b) FT-IR spectra of all the samples, and XPS spectra of (c) B 1s, (d) N 1s and (e) C 1s for the BN and BCN-2.

The element valence state was investigated by X-ray photoelectron spectroscopy (XPS). As shown in Fig. 2c, the B 1s spectrum of the pure BN shows a major peak at 190.5 eV (B–N bond) and a weak peak at 192.0 eV (B–O bond). For BCN-2, the three peaks located at 190.5, 190.2 and 192.3 eV, respectively, indicate the presence of B–N, B–C and B–O bonds in BCN-2.[39] The N 1s spectrum (Fig. 2d) of BCN-2 shows the binding energy of the N–C and N–B bonds corresponding to 398.4 and 397.9 eV while pure BN has only one binding energy at 398.2 eV corresponding to B–N.[40] The C 1s spectrum (Fig. 2e) of BCN-2 shows four peaks at 288.9, 286.4, 284.8 and 284.5 eV corresponding to the C=O bond, C–N bond, graphitic carbon (C=C) and C–B bond, respectively.[41] The presence of a small peak at 284.8 eV in the C 1s of pure BN is mainly due to contaminants during the testing process. The formation of bonds associated with the C proves that carbon is indeed incorporated into the B–N domain.

A part of the carbon evaporated during the high-temperature pyrolysis process, which caused abundant pore structures. SEM and TEM images reveal that BCN possesses a nanosheet-like morphology feature (Fig. 3a and b). Furthermore, the element mapping images prove that the carbon is uniformly incorporated into the boron nitride (Fig. 3c–f). The N_2 adsorption–desorption isotherms (Fig. 3g) and the pore size distribution (Fig. 3h) were used to investigate the specific surface area and the pore structures (summarized in Table S1†). The specific surface area of BCN increased from 91 $m^2 g^{-1}$ to 915 $m^2 g^{-1}$ and the pore volume increased from 0.06 $cm^3 g^{-1}$ to 0.4 $cm^3 g^{-1}$ with the increasing addition of glucose in the precursor.

3.2 The local electronic configuration and band structure of BCN

The electronic configuration of the synthesized BCN was investigated with the help of electron paramagnetic resonance (EPR) spectra. Fig. 4a shows BCN has a Lorentzian line signal with a *g* value of 2.0027 while no EPR signals are observed in the pure BN sample, which indicates an unpaired electron is formed in BCN. When the C atom is integrated into B–N, the delocalized π bond is formed in the C atom because each C and N atom has one or a pair of unbonded electrons in their unhybridized p-orbitals.[33,36] This delocalized π bond enhances

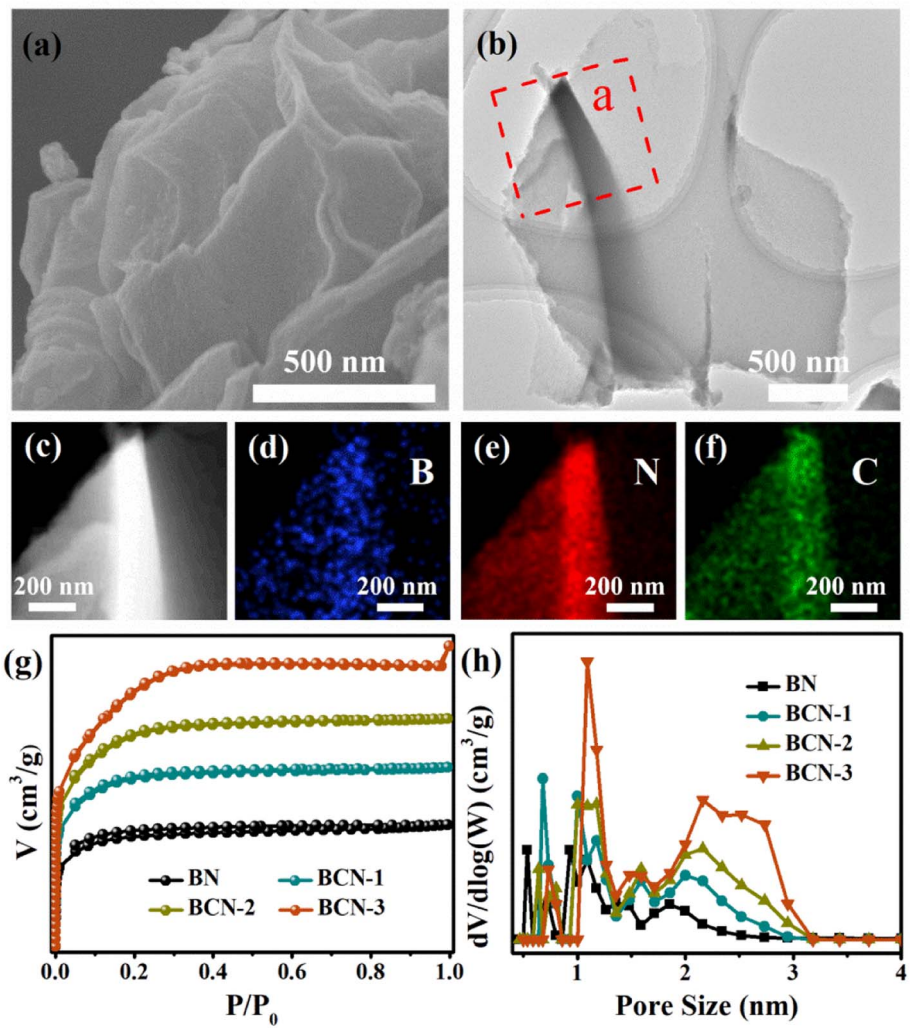

Fig. 3 (a) SEM image of the BCN-2 sample, (b) TEM image of the BCN-2 sample, (c–f) element mapping images of the BCN-2 sample, (g) N_2 adsorption–desorption isotherm plots of all samples and (h) the pore size distribution of all samples.

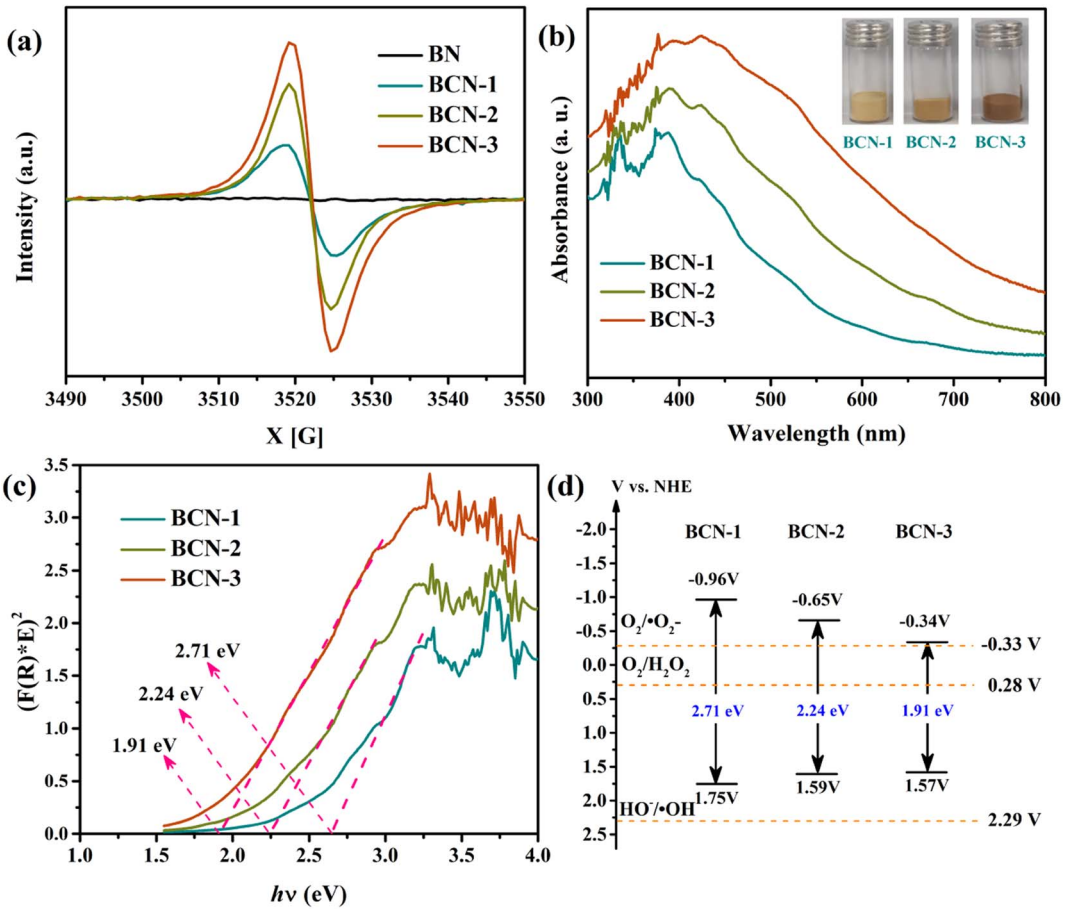

Fig. 4 (a) EPR spectra of all samples, (b) UV-vis DRS patterns of all BCN samples, (c) Tauc plots of all BCN samples and (d) the band structure of all BCN samples.

the light absorption capacity of BCN and reduces the band gap. Meanwhile, the EPR signal value of BCN increases with increasing carbon content, proving that more unpaired electrons are formed. The UV-visible diffuse reflectance absorption (UV-vis DRS) spectrum is used to study the upgraded electronic states of BN and light absorption. As shown in Fig. 4b, both BN and BCN show a distinct absorption band at 200–300 nm which is attributed to σ electron excitation (σ → σ*) in the B–N bond.[42] After introducing carbon, an obvious absorption edge around 300–430 nm appeared, which derives from π electron excitation (π → π*) in BCN samples.[33] There is no excitation of π electrons in pristine BN because N atoms generally have higher electronegativity than B atoms.[43] Meanwhile, the photograph shows that the white BN gradually turns light yellow, and finally turns dark yellow with increasing carbon content. As shown in Fig. 4c, the band gaps are 1.91, 2.24 and 2.71 eV for samples BCN-3, BCN-2 and BCN-1, and the corresponding CB potentials are −0.52, −0.83 and −1.15 eV, respectively (Fig. S1†). The band structures of all BCN are exhibited in Fig. 4d. The incorporation of carbon improves the light absorption of BN by reducing the band gap, as demonstrated by these findings.

3.3 Charge separation and migration

In a typical photocatalytic process, the separation and migration of photogenerated charges are also important factors affecting photocatalytic performance besides the band structure of semiconductor catalysts. The solid-state EPR spectrum (Fig. S2†) shows that the signal at a *g* value of 2.0 became stronger under visible light illumination, which reveals the generation and delivery of photo-introduced electrons in BCN.[44] Photoelectrochemical (PEC) testing was used to study the separation and migration of photogenerated charges. The transient photocurrent–time curves of samples were recorded by intermittent on–off cycles of visible light irradiation. There is no signal of photocurrent in BN because it cannot absorb visible light (Fig. 5a). All BCN samples show a distinct photocurrent response and the photocurrent density increased with increasing carbon content. The charge migration ability of the BCN electrode was further studied by electrochemical impedance spectroscopy (EIS). Fig. 5b shows the diameter of the semicircle in the EIS Nyquist plots presents a trend of BN > BCN-1 > BCN-3 > BCN-2, indicating the impedance reduction of BCN after carbon incorporation in BN.

The trapping, migration, and recombination of photogenerated charges of BCN were studied with the help of fluorescence (PL) spectra. As shown in Fig. 5c, BCN-1 exhibits

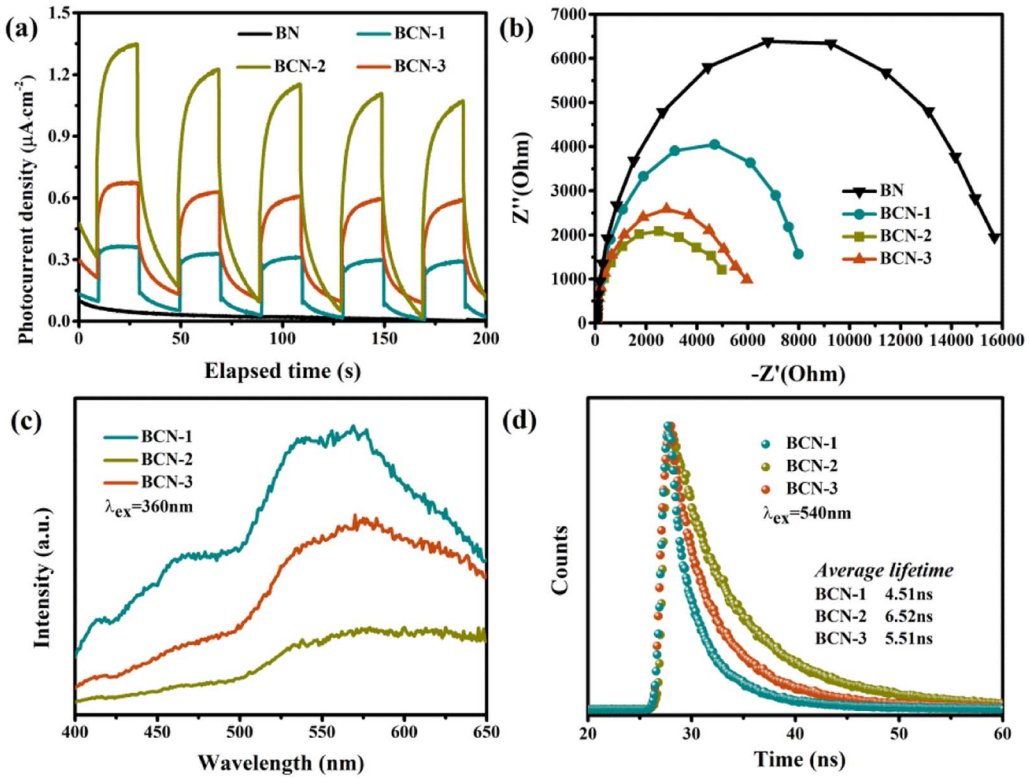

Fig. 5 (a) Transient photocurrent response curve of all samples, (b) electrochemical impedance spectroscopy (EIS) patterns of all BCN samples, (c) PL spectra of the BCN samples and (d) time-resolved photoluminescence (TRPL) spectra of all BCN samples.

a strong fluorescence emission signal in the range of 450 nm to 550 nm under the excitation of 360 nm light. The BCN-2 sample shows the lowest PL signal, indicating the minimum recombination rate of photogenerated carriers. The higher PL signal of BCN-3 than BCN-2 indicates that excessive carbon is not conducive to the separation and migration of photogenerated carriers. Time-resolved PL spectra (Fig. 5d) show that BCN-2 has a longer PL decay time and the calculated average lifetimes of BCN-3, BCN-2 and BCN-1 are 5.51, 6.52 and 4.51 ns, respectively. A small amount of carbon causes less photogenerated charge due to the weak absorption capacity of light, while excess carbon leads to the formation of more defects and leads to increased photogenerated carrier recombination. The above results indicate regulating optimal light absorption and photogenerated charge separation ability is achieved by optimizing the carbon content in BCN samples.

3.4 The photocatalytic performance of BCN catalysts

Typical photocatalytic oxidation of sulfur-containing gas (H_2S) was carried out in a continuous reaction unit using standard air as the source of oxygen. Before illumination, the feed gas was pumped through BCN in the dark state for a while to ensure reactant molecules reach a dynamic equilibrium of adsorption–desorption on the catalyst surface. As shown in Fig. 6a, BN exhibits only little photocatalytic activity (H_2S removal efficiency <7%) under illumination, while all the BCN samples show a significant activity for photocatalytic removal of H_2S. In addition, the carbon content shows an essential effect on the activity of BCN. The BCN-1 sample containing a small amount of carbon showed a rapid decrease in activity as the reaction proceeded, although it displayed a better H_2S removal efficiency (about 95%) at the beginning of the light irradiation. This may be because the active sites in BCN that play a major catalytic role are carbon-related, while the small amount of carbon-related active sites in sample BCN-1 are quickly covered by the product as the reaction time increases. The optimized sample of BCN-2 not only exhibits the best H_2S removal efficiency (>97%) but also maintains high activity for 80 min. More carbon provides more active sites as well as improved light absorption performance and photogenerated charge separation efficiency, so BCN-2 exhibits the best photocatalytic performance. It is worth noting that excessive carbon incorporation produces more defects in the BCN sample resulting in low photogenerated charge separation efficiency, thus BCN-3 shows low photocatalytic activity (<70%).

A light-shielding experiment was used to verify the relation between H_2S removal and illumination. As shown in Fig. 6b, within six alternating light on–off cycle processes, the H_2S removal only occurs in the light while not occurring in the dark. This proves that the removal of H_2S is driven by light. Meanwhile, the photocatalytic experiments were performed under different monochromatic wavelengths to further investigate the dependency of H_2S removal with illumination. To ensure the accuracy and reasonable comparison result, the activity values of every point wavelength were normalized by the optical power density (detailed information in Table S2†). Fig. 6c shows that

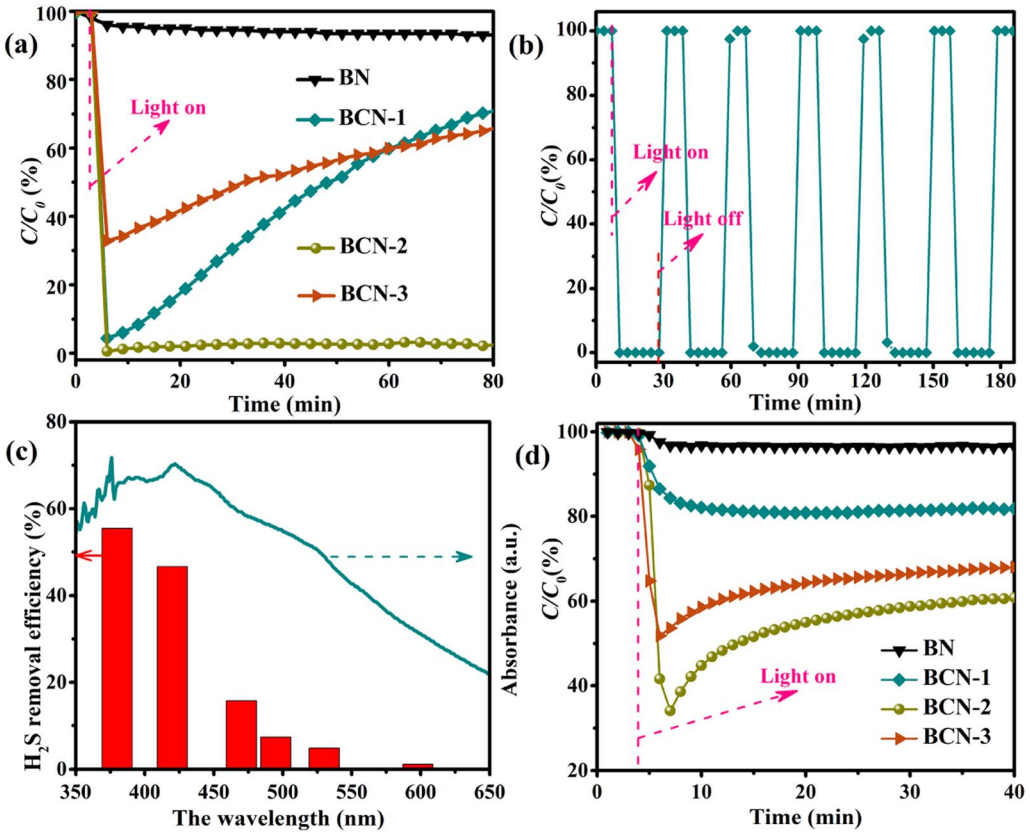

Fig. 6 (a) Photocatalytic H_2S removal activity of all the samples, (b) photocatalytic activity testing of the BCN-2 sample under light on–off cycles, (c) photocatalytic activity testing of the BCN-2 sample under different monochromatic wavelengths and (d) photocatalytic NO purification of all the samples.

the H_2S removal efficiency of the BCN-2 sample decreases from 55.45% to 1.14% as the wavelength increases from 380 nm to 598 nm. This confirms a distinct correlation between the removal of H_2S and the light absorption of BCN.

For further evaluating the photocatalytic performance of the BCN sample, a long-time stability test was performed (shown in Fig. S3†). It shows that the photocatalytic removal of H_2S remained close to 100% over BCN-2 under continuous illumination within 250 min and then decreased slightly (about 7.3%) under continuous illumination for 4 h. This may result from the poisoning of the active sites or coverage by the products. Importantly, the activity of the BCN can be restored by annealing at 750 °C in an NH_3 atmosphere because of the regeneration of active sites during the annealing process. Moreover, Fig. S4 and S5† show that the XRD and FTIR of the used BCN show no obvious changes compared to those of the fresh sample. This demonstrates the excellent stability and regeneration of BCN in the process of photocatalytic removal of H_2S.

For further exploration of the application of BCN in the photocatalytic removal of acid gases, the photocatalytic removal of typical nitrite-containing gas (NO) was also performed. The NO removal efficiency of BN is almost negligible (Fig. 6d). Obviously, the concentration of NO decreases significantly over BCN samples after turning on the light. In addition, the NO removal efficiency of BCN-1 and BCN-2 increases from 20% to 60% with increasing carbon content, while the activity of BCN-3 decreases to 40% with carbon excess. This result is consistent with the trend of photocatalytic removal of H_2S, indicating that BCN as an excellent photocatalyst has potential for photocatalytic removal of gaseous contaminants containing sulfur and nitrate.

3.5 Activation of gas molecules and photocatalytic mechanism

A programmed temperature-up desorption test was used to investigate the chemical adsorption of H_2S and O_2 over the BCN sample. As shown in Fig. 7a, the obvious TCD signal appeared at 110 °C corresponding to the desorbed H_2S. This signal increases with increasing carbon content, which may be caused by the increased specific surface area of the BCN sample. Fig. 7b shows a very weak desorption signal for oxygen on the BN sample while showing a strong desorption signal at 140 °C on the BCN sample. These results reveal that incorporating carbon into BN improves the chemical adsorption of O_2 and H_2S.

To further investigate the behavior of reactant molecules on the BCN surface during photocatalysis, an DRIFTS test was performed. The BCN sample was pretreated in a high-purity argon atmosphere at 200 °C for 2 hours before testing to remove the surface attachment. As shown in Fig. 7c, when light

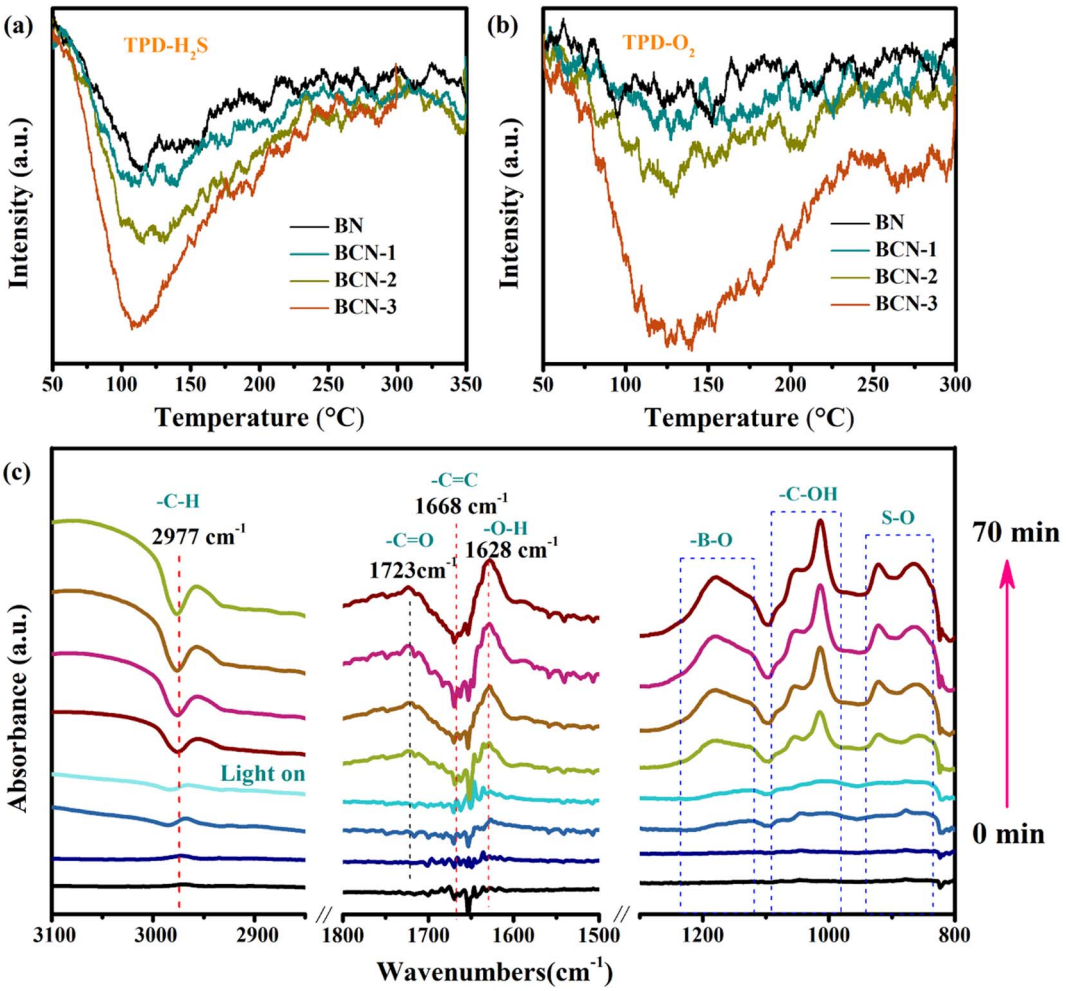

Fig. 7 (a) The temperature-programmed desorption curves of H_2S for all the samples, (b) the temperature-programmed desorption curves of O_2 for all the samples, (c) DRIFTS test for photocatalytic H_2S removal over the BCN-2 sample.

is turned on, the positive peak at 1723 cm^{-1} appears and increases in intensity with increasing light time, which corresponds to the –C═O stretching vibration modes. This peak derives from the O_2 molecules adsorbed on the carbon attached to the carbon ring.[36,45] Correspondingly, the effecting C═C stretching vibration mode shifts from 1668 cm^{-1} to 1628 cm^{-1}

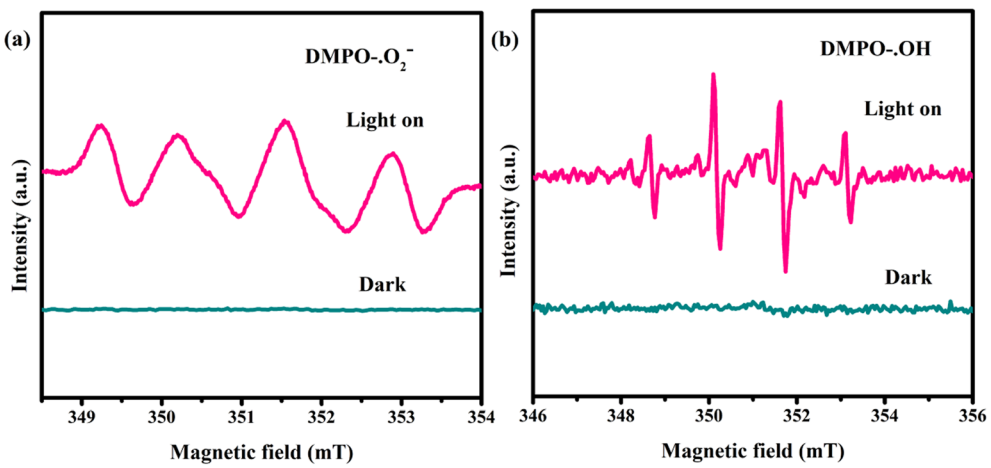

Fig. 8 DMPO EPR spin-trapping of the BCN-2 sample for $^{\bullet}O_2^-$ (a) and $^{\bullet}OH^-$ (b) radicals.

and corresponds to –C–H vibrations observed as negative peaks at 2977 cm^{-1}.[46] This agrees with the experimental results demonstrating that oxygen activation is indeed related to carbon in the BCN. In addition, high concentrations of H_2S gas were used to investigate the adsorption of H_2S because the infrared vibration signal of HS^- is very weak. A weak peak appeared at 2580 cm^{-1} corresponding to an HS^- characteristic peak, proving H_2S can dissociate on the BCN surface (Fig. S6†).[47]

The reactive oxygen species were investigated with the help of DMPO ESR spin-trapping spectra (Fig. 8). Any EPR signal does not appear when BN is dispersed in methanol or aqueous solution under visible light, because BN cannot be excited by visible light. Markedly, BCN in the ethanol dispersion shows four obvious signals with an intensity ratio of 1 : 1 : 1 : 1 under illumination, which is consistent with what is reported for the superoxide radical ($^{\bullet}O_2^-$) (Fig. 8a).[15,16] The photogenerated electrons of BCN can activate oxygen to generate direct $^{\bullet}O_2^-$ because the CB potential of BCN (<−0.52 eV) is more negative than the reduction potential of $O_2/^{\bullet}O_2^-$ (−0.33 eV) (eqn (1) and (2)).[17] In addition, Fig. 8b shows four strong signal peaks with an intensity ratio of 1 : 2 : 2 : 1 in the aqueous solution of BCN, which is assigned to light-induced hydroxyl radicals ($^{\bullet}OH$).[15,16] Note that the photogenerated holes from BCN cannot directly oxidize H_2O or HO^- to the $^{\bullet}OH$ radical due to the oxidation potentials of $HO^-/^{\bullet}OH$ and $H_2O/^{\bullet}OH$ (1.99 and 2.37 eV) being more positive than the VB potential of BCN (<1.56 eV).[17] The detected $^{\bullet}OH$ radical signal in Fig. 8 derives from the pathway of $^{\bullet}O_2^- \rightarrow H_2O_2 \rightarrow {}^{\bullet}OH$ (eqn (3)–(6)).[48,49]

$$h\nu + BCN \rightarrow h^+ + e^- \quad (1)$$

$$O_2 + e^- \rightarrow {}^{\bullet}O_2^- \quad (2)$$

$$H^+ + {}^{\bullet}O_2^- \rightarrow {}^{\bullet}HO_2 \quad (3)$$

$$^{\bullet}HO_2 + HO_2^{\bullet} \rightarrow H_2O_2 + O_2 \quad (4)$$

$$O_2 + 2e^- + 2H^+ \rightarrow H_2O_2 \quad (5)$$

$$e^- + H_2O_2 \rightarrow {}^{\bullet}OH + OH^- \quad (6)$$

In a typical photocatalytic process, H_2S molecules first adsorbed onto the surface of BCN, dissociating into HS^- and H^+ (eqn (7)). The photogenerated holes can oxidize dissociated HS^- to yield elemental sulfur, which is further oxidized to SO_2 by $^{\bullet}OH$ radicals (eqn (8) and (9)).[50] Then oxygen readily oxidizes SO_2 to SO_3 and subsequently reacts with H_2O to produce sulfuric acid (eqn (10) and (11)).[51] The generated sulfuric acid reacts with the basic groups of the BCN surface to produce sulfate species (eqn (12)).[52] In another pathway, dissociated HS^- is directly reacted with $^{\bullet}OH$ to yield sulfate species (eqn (13)).[14,53] As mentioned above, the residual S species on the surface of BCN after the stability test is analyzed by XPS to investigate the products of H_2S oxidation. Two peaks at 169.2 eV and 163.9 eV are shown in the S 2p spectrum and they are attributed to SO_4^{2-} and elemental sulfur, respectively (Fig. S7†).[4,20] In addition,

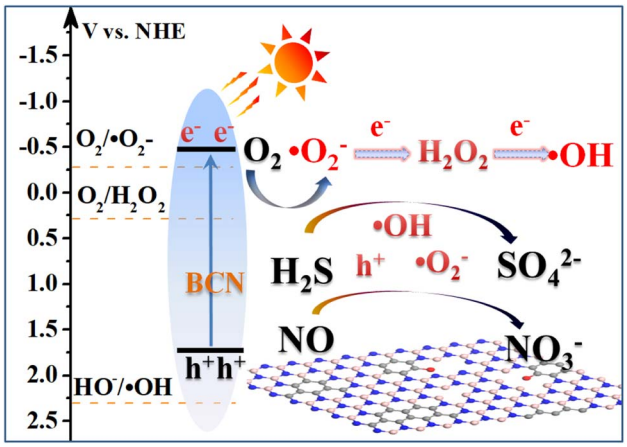

Fig. 9 Schematic of photocatalytic removal of gas contaminants over the BCN catalyst.

there are no other gaseous sulfur components except for detected SO_2 in the exhaust gas.

$$H_2S_{gas} \rightarrow HS_{ads}^- + H^+ \quad (7)$$

$$HS_{ads}^- + h^+ \rightarrow S_{ads} + H^+ \quad (8)$$

$$S_{ads} + {}^{\bullet}OH \rightarrow 2SO_{2ads} \quad (9)$$

$$SO_{2ads} + O_2 \rightarrow 2SO_{3ads} \quad (10)$$

$$SO_{3ads} + H_2O \rightarrow H_2SO_{4ads} \quad (11)$$

$$H_2SO_{4ads} + OH^- \rightarrow SO_4^{2-} + 2H_2O \quad (12)$$

$$HS_{ads}^- + 8{}^{\bullet}OH \rightarrow SO_4^{2-} + H^+ + 4H_2O \quad (13)$$

Thus a possible photocatalytic removal of gas contaminants over BCN is proposed. To begin with, the transformation of BN from a ceramic insulator to a semiconductor is achieved by carbon doping. The band structure of BCN is further optimized to enhance the separation ability of photogenerated charges. As shown in Fig. 9, under visible light, BCN is excited to generate photogenerated electrons and holes, which follow migration to the BCN surface. Then, oxygen molecules are activated by the pathway of $^{\bullet}O_2^- \rightarrow H_2O_2 \rightarrow {}^{\bullet}OH$. The acidic gas molecules preferentially react with $^{\bullet}OH$ radicals to generate the corresponding strong acid salts. Moreover, photogenerated holes and $^{\bullet}O_2^-$ may also be involved in the oxidation of parts of the acidic gas molecules. Eventually, acidic gaseous pollution is ultimately removed through a photocatalytic process.

4. Conclusion

Herein, ceramic BN as a semiconductor material with the absorption of visible light was applied in photocatalytic removal of acid gas. More importantly, controllable regulation of the band structure of the BCN catalyst is realized by controlling the amount of carbon incorporation, which increases the capture capacity of visible light and the separation ability of

photogenerated charge. This novel non-metallic based photocatalyst overcomes the defects of traditional metal catalysts that are prone to sulfur poisoning and exhibits excellent performance that directly handles the low concentration of acid gas in the continuous operation process. This work could provide a fresh idea to eliminate acid gas and deepen the mechanistic comprehension of photocatalytic degradation of gas contaminants.

Author contributions

Hao Yang: investigation, methodology, conceptualization, writing – original draft. Libin Zeng: investigation, formal analysis, validation. Jiali Wang: conceptualization, writing – review & editing. Can Yang: supervision, funding acquisition, project administration, writing – review and editing.

Conflicts of interest

There are no conflicts of interest to declare.

Acknowledgements

This work was financially supported by the National Key Technologies R&D Program of China (2018YFA0209301), the National Natural Science Foundation of China (222072027, U1905214, 21425309, 21761132002, 21961142019, 5261130353 and 21976177), the Chang Jiang Scholars Program of China (T2016147) and the 111 Project (D16008). C. Y. also acknowledges the support from the Eyas Program of Fujian Province.

References

1 Q. Zhou, J. Yang, M. Liu, Y. Liu, S. Sarnat and J. Bi, Toxicological risk by inhalation exposure of air pollution emitted from China's municipal solid waste incineration, *Environ. Sci. Technol.*, 2018, **52**, 11490–11499.

2 A. Pieplu, O. Saur and J. Lacxlley, Claus catalysis and H_2S selective oxidation, *Catal. Rev.: Sci. Eng.*, 1998, **40**, 409–450.

3 Y. Liu, T. Bisson, H. Yang and Z. Xu, Recent developments in novel sorbents for flue gas clean up, *Fuel Process. Technol.*, 2010, **91**, 1175–1197.

4 X. Zhang, Y. Tang, S. Qu, J. Da and Z. Hao, H_2S-Selective catalytic oxidation: catalysts and processes, *ACS Catal.*, 2015, **5**, 1053–1067.

5 R. Cai, X. Ke, Y. Huang, S. Zhu, Y. Li, J. Cai, H. Yang, J. Lyu and M. Zhang, Applications of ultrafine limestone sorbents for the desulfurization process in CFB boilers, *Environ. Sci. Technol.*, 2019, **53**, 13514–13523.

6 A. Okab, Z. Jabbar, B. Graimed, A. Alwared, S. Ammar and M. Hussein, A comprehensive review highlights the photocatalytic heterojunctions and their superiority in the photo-destruction of organic pollutants in industrial wastewater, *Inorg. Chem. Commun.*, 2023, **158**, 111503.

7 V. Pârvulescu, P. Grange and B. Delmon, Catalytic removal of NO, *Catal. Today*, 1998, **46**, 233–316.

8 B. Graimed, Z. Jabbar, M. Alsunbuli, S. Ammar, S. Hamood, A. Taher and D. Sabit, Rational design of 1D TaON nanofibrous network decorated 2D BiOBr nanosheets for sustainable photocatalytic detoxification of antibiotics in wastewater via S-scheme heterostructure system, *J. Water Process Eng.*, 2023, **54**, 104059.

9 Z. H. Jabbar, B. H. Graimed, M. M. Alsunbuli and D. Sabit, Developing a magnetic bismuth-based quaternary semiconductor boosted by plasmonic action for photocatalytic detoxification of Cr(VI) and norfloxacin antibiotic under simulated solar irradiation: Synergistic work and radical mechanism, *J. Alloys Compd.*, 2023, **958**, 170521.

10 M. Schreck and M. Niederberger, Photocatalytic gas phase reactions, *Chem. Mater.*, 2019, **31**, 597–618.

11 A. Okab, Z. Jabbar, B. Graimed, M. Alsunbuli and M. M-Ridha, Synergistic behavior between the plasmonic Ag metal and the mesoporous β-Bi_2O_3/SiO_2 heterostructure for the photocatalytic destruction of bacterial cells under simulated sunlight illumination: Schottky junction electron-transfer pathway, *Environ. Nanotechnol., Monit. Manage.*, 2023, **20**, 100811.

12 Z. Jabbar, B. Graimed, S. Ammar, M. Alsunbuli, S. Hamood, H. Najm and A. Taher, Design and construction of a robust ternary Bi_5O_7I/$Cd_{0.5}Zn_{0.5}S$/CuO photocatalytic system for boosted photodegradation of antibiotics via dual-S-scheme mechanisms: environmental factors and degradation intermediates, *Environ. Res.*, 2023, **234**, 116554.

13 B. Graimed, A. Okab, Z. Jabbar, M. A. Issa and S. Ammar, Highly stable β-Bi_2O_3/Ag decorated nanosilica as an efficient Schottky heterojunction for ciprofloxacin photodegradation in wastewater under LED illumination, *Mater. Sci. Semicond. Process.*, 2023, **156**, 107303.

14 H. Sheng, D. Chen, N. Li, Q. Xu, H. Li, J. He and J. Lu, Urchin-inspired TiO_2@MIL-101 double-shell hollow particles: adsorption and highly efficient photocatalytic degradation of hydrogen sulfide, *Chem. Mater.*, 2017, **29**, 5612–5616.

15 W. Cui, J. Li, F. Dong, Y. Sun, G. Jiang, W. Cen, S. Lee and Z. Wu, Highly efficient performance and conversion pathway of photocatalytic NO oxidation on SrO-clusters@amorphous carbon, *Environ. Sci. Technol.*, 2017, **51**, 10682–10690.

16 F. Dong, Z. Wang, Y. Li, W. Ho and S. Lee, Immobilization of polymeric g-C_3N_4 on structured ceramic foam for efficient visible light photocatalytic air purification with real indoor illumination, *Environ. Sci. Technol.*, 2014, **48**, 10345–10353.

17 X. Li, J. Yu and M. Jaronie, Hierarchical photocatalysts, *Chem. Soc. Rev.*, 2016, **45**, 2603–2636.

18 Z. H. Jabbar, A. A. Okab, B. H. Graimed, M. A. Issa and S. Ammar, Fabrication of g-C_3N_4 nanosheets immobilized Bi_2S_3/Ag_2WO_4 nanorods for photocatalytic disinfection of Staphylococcus aureus cells in wastewater: dual S-scheme charge separation pathway, *J. Photochem. Photobiol., A*, 2023, **438**, 114556.

19 X. Wang, K. Maeda, A. Thomas, K. Takanabe, G. Xin, J. Carlsson, K. Domen and M. Antonietti, A Metal-free

polymeric photocatalyst for hydrogen production from water under visible light, *Nat. Mater.*, 2009, **8**, 76–82.

20 L. Shen, G. Lei, Y. Fang, Y. Cao, X. Wang and L. Jiang, Polymeric carbon nitride nanomesh as an efficient and durable metal-free catalyst for oxidative desulfurization, *Chem. Commun.*, 2018, **54**, 2475–2478.

21 Z. Jabbar, B. Graimed, A. Okab, M. Alsunbuli and R. Alhusseiny, Construction of 3D flower-like Bi5O7I/Bi/Bi2WO6 heterostructure decorated NiFe2O4 nanoparticles for photocatalytic destruction of Levofloxacin in aqueous solution: Synergistic effect between S-scheme and SPR action, *J. Photochem. Photobiol., A*, 2023, **441**, 114734.

22 M. Xu, T. Liang, M. Shi and H. Chen, Graphene-like two-dimensional materials, *Chem. Rev.*, 2013, **113**, 3766–3798.

23 Q. Weng, X. Wang, X. Wang, Y. Bando and D. Golberg, Functionalized hexagonal boron nitride nanomaterials: emerging properties and applications, *Chem. Soc. Rev.*, 2016, **45**, 3989–4012.

24 J. Yin, J. Li, Y. Hang, Y. Jin, G. Tai, X. Li, Z. Zhang and W. Guo, Boron nitride nanostructures: fabrication, functionalization and applications, *Small*, 2016, **12**, 2942–2968.

25 S. Meng, X. Ye, X. Ning, M. Xie, X. Fu and S. Chen, Selective oxidation of aromatic alcohols to aromatic aldehydes by BN/metal sulfide with enhanced photocatalytic activity, *Appl. Catal., B*, 2016, **182**, 356–368.

26 M. Zhou, S. Wang, P. Yang, C. Huang and X. Wang, Boron carbon nitride semiconductors decorated with CdS Nanoparticles for photocatalytic reduction of CO_2, *ACS Catal.*, 2018, **8**, 4928–4936.

27 A. Bhattacharya, S. Bhattacharya and G. P. Das, Band gap engineering by functionalization of BN sheet, *Phys. Rev. B: Condens. Matter Mater. Phys.*, 2012, **85**, 035415.

28 X. Li, J. Zhao and J. Yang, Semihydrogenated BN Sheet: a promising visible-light driven photocatalyst for water splitting, *Sci. Rep.*, 2013, **3**, 1858.

29 Q. Weng, Y. Ide, X. Wang, X. Wang, C. Zhang, X. Jiang, Y. Xue, P. Dai, K. Komaguchi, Y. Bando and D. Golberg, Design of BN porous sheets with richly exposed (002) plane edges and their application as TiO_2 visible light sensitizer, *Nano Energy*, 2015, **16**, 9–27.

30 Q. Weng, L. Zeng, Z. Chen, Y. Han, K. Jiang, Y. Bando and D. Golberg, Hydrogen storage in carbon and oxygen Co-doped porous boron nitrides, *Adv. Funct. Mater.*, 2021, **31**, 2007381.

31 D. Portehault, C. Giordano, C. Gervais, I. Senkovska, S. Kaskel, C. Sanchez and M. Antonietti, High-surface-area nanoporous boron carbon nitrides for hydrogen storage, *Adv. Funct. Mater.*, 2010, **20**, 1827–1833.

32 M. Du, X. Li, A. Wang, Y. Wu, X. Hao and M. Zhao, One-step exfoliation and fluorination of boron nitride nanosheets and a study of their magnetic properties, *Angew. Chem., Int. Ed.*, 2014, **53**, 3645–3649.

33 C. Huang, C. Chen, M. Zhang, L. Lin, X. Ye, S. Lin, M. Antonietti and X. Wang, Carbon-doped BN nanosheets for metal-free photoredox catalysis, *Nat. Commun.*, 2015, **6**, 7698.

34 Z. Luo, Y. Fang, M. Zhou and X. Wang, A borocarbonitride ceramic aerogel for photoredox catalysis, *Angew. Chem., Int. Ed.*, 2019, **58**, 6033–6037.

35 M. Zhou, Z. Chen, P. Yang, S. Wang, C. Huang and X. Wang, Hydrogen reduction treatment of boron carbon nitrides for photocatalytic selective oxidation of alcohols, *Appl. Catal., B*, 2020, **276**, 118916.

36 W. Qu, P. Wang, M. Gao, J. Hasegawa, Z. Shen, Q. Wang, R. Li and D. Zhang, Delocalization effect promoted the indoor air purification via directly unlocking the ring-opening pathway of toluene, *Environ. Sci. Technol.*, 2020, **54**, 9693–9701.

37 Y. Shi, C. Hamsen, X. Jia, K. Kim, A. Reina, M. Hofmann, A. Hsu, K. Zhang, H. Li, Z. Juang, D. Mresselhaus, L. Li and J. Kong, Synthesis of few-layer hexagonal boron nitride thin film by chemical vapor deposition, *Nano Lett.*, 2010, **10**, 4134–4139.

38 R. Geick and C. Perry, Normal modes in hexagonal boron nitride, *Phys. Rev.*, 1966, **146**, 543–547.

39 W. Lei, D. Portehault, R. Dimova and M. Antonietti, Boron carbon nitride nanostructures from salt melts: tunable water-soluble phosphors, *J. Am. Chem. Soc.*, 2011, **133**, 7121–7127.

40 H. Li, S. Zhu, M. Zhang, P. Wu, J. Pang, W. Zhu, W. Jiang and H. Li, Tuning the chemical hardness of boron nitride nanosheets by doping carbon for enhanced adsorption capacity, *ACS Omega*, 2017, **2**, 5385–5394.

41 S. Kim, J. Park, H. Choi, J. Ahn, J. Hou and H. Kang, X-ray photoelectron spectroscopy and first principles calculation of BCN nanotubes, *J. Am. Chem. Soc.*, 2007, **129**, 1705–1716.

42 G. Gao, A. Mathkar, E. Martins, D. Galvão, D. Gao, P. Autreto, C. Sun, L. Cai and P. Ajayan, Designing nanoscaled hybrids from atomic layered boron nitride with silver nanoparticle deposition, *J. Mater. Chem. A*, 2014, **2**, 3148–3154.

43 W. Wang, H. Zhang, S. Zhang, Y. Liu, G. Wang, C. Sun and H. Zhao, Potassium-Ion-assisted regeneration of active cyano groups in carbon nitride nanoribbons: Visible-light-driven photocatalytic nitrogen reduction, *Angew. Chem., Int. Ed.*, 2019, **58**, 16644–16650.

44 J. Li, X. Dong, Y. Sun, G. Jiang, Y. Chu, S. Lee and F. Dong, Tailoring the rate-determining step in photocatalysis via localized excess electrons for efficient and safe air cleaning, *Appl. Catal., B*, 2018, **239**, 187–195.

45 M. Wang, M. Shen, X. Jin, J. Tian, M. Li, Y. Zhou, L. Zhang, Y. Li and J. Shi, Oxygen vacancy generation and stabilization in CeO_{2-x} by Cu introduction with improved CO_2 photocatalytic reduction activity, *ACS Catal.*, 2019, **9**, 4573–4581.

46 G. Mittal, K. Rhee, S. Park and D. Hui, Generation of the pores on graphene surface and their reinforcement effects on the thermal and mechanical properties of chitosan-based composites, *Composites, Part B*, 2017, **114**, 348–355.

47 A. Datta and R. Cavell, Claus Catalysis. 2. An FTIR study of the adsorption of H_2S on the alumina catalyst, *J. Phys. Chem.*, 1985, **89**, 450–454.

48 P. Chen, H. Wang, H. Liu, Z. Ni, J. Li, Y. Zhou and F. Dong, Directional electron delivery and enhanced reactants

activation enable efficient photocatalytic air purification on amorphous carbon nitride co-functionalized with O/La, *Appl. Catal., B*, 2019, **242**, 19–30.

49 M. Hayyan, M. Hashim and I. AlNashef, Superoxide Ion: Generation and chemical implications, *Chem. Rev.*, 2016, **116**, 3029–3085.

50 R. Portela, M. Canela, B. Sánchez, F. Marques, A. Stumbo, R. Tessinari, J. Coronado and S. Suárez, H_2S photodegradation by TiO_2/M-MCM-41 (M=Cr or Ce): deactivation and by-product generation under UV-A and visible light, *Appl. Catal., B*, 2008, **84**, 643–650.

51 C. Liu, R. Zhang, S. Wei, J. Wang, Y. Liu, M. Li and R. Liu, Selective removal of H_2S from biogas using a regenerable hybrid TiO_2/zeolite composite, *Fuel*, 2015, **157**, 183–190.

52 A. Alonso-Tellez, D. Robert, N. Keller and V. Keller, A parametric study of the UV-A photocatalytic oxidation of H_2S over TiO_2, *Appl. Catal., B*, 2012, **115–116**, 209–218.

53 G. Zhang, H. Sheng, D. Chen, N. Li, Q. Xu, H. Li, J. He and J. Lu, Hierarchical titanium dioxide Nanowire/Metal–Organic Framework/Carbon nanofiber membranes for highly efficient photocatalytic degradation of hydrogen sulfide, *Chem. – Eur. J.*, 2018, **24**, 15019–15025.